



Open Archive TOULOUSE Archive Ouverte (OATAO)

OATAO is an open access repository that collects the work of Toulouse researchers and makes it freely available over the web where possible.

This is an author-deposited version published in : <http://oatao.univ-toulouse.fr/>
Eprints ID : 8538

To link to this article : DOI:10.1364/OE.21.006609
URL : <http://dx.doi.org/10.1364/OE.21.006609>

To cite this version :

Wang, Yunshan and Plouraboué, Franck and Chang, Hsueh-Chia
Broadband converging plasmon resonance at a conical nanotip.
(2013) Optics Express, vol. 21 (n° 5). pp. 6609-6617. ISSN 1094-4087

Any correspondence concerning this service should be sent to the repository administrator: staff-oatao@listes.diff.inp-toulouse.fr

Broadband converging plasmon resonance at a conical nanotip

Yunshan Wang¹, Franck Plouraboue,² and Hsueh-Chia Chang^{1,*}

¹*Department of Chemical and Biomolecular Engineering, University of Notre Dame, Notre Dame, Indiana 46556, USA*

²*Universit de Toulouse, INPT, UPS, IMFT (Institut de Mcanique des Fluides de Toulouse), Alls Camille Soula, F-31400 Toulouse, France and CNRS, IMFT, F-31400 Toulouse, France*

[*hchang@nd.edu](mailto:hchang@nd.edu)

Abstract: We propose an analytical theory which predicts that Converging Plasmon Resonance (CPR) at conical nanotips exhibits a red-shifted and continuous band of resonant frequencies and suggests potential application of conical nanotips in various fields, such as plasmonic solar cells, photothermal therapy, tip-enhanced Raman and other spectroscopies. The CPR modes exhibit superior confinement and ten times broader scattering bandwidth over the entire solar spectrum than smooth nano-structures. The theory also explicitly connects the optimal angles and resonant optical frequencies to the material permittivities, with a specific optimum half angle that depends only on the real permittivity for high-permittivity and low-loss materials.

References and links

1. V. Ferry, J. Munday, and H. Atwater, "Design considerations for plasmonic photovoltaics," *Adv. Mater.* **22**, 4794–4808 (2010).
2. X. Lu, M. Rycenga, S. Skrabalak, B. Wiley, and Y. Xia, "Chemical synthesis of novel plasmonic nanoparticles," *Annu. Rev. Phys. Chem.* **60**, 167–192 (2009).
3. C. Lee, S. Bae, S. Mobasser, and H. Manohara, "A novel silicon nanotips antireflection surface for the micro sun sensor," *Nano Lett.* **5**, 2438–2442 (2005).
4. A. R. Parker and H. E. Townley, "Biomimetics of photonic nanostructures," *Nat. Nanotechnol.* **2**, 347–353 (2007).
5. A. V. Goncharenko, H. C. Chang, and J. K. Wang, "Electric near-field enhancing properties of a finite-size metal conical nano-tip," *Ultramicroscopy* **107**, 151–157 (2007).
6. X. Huang, I. H. El-Sayed, W. Qian, and M. A. El-Sayed, "Cancer cell imaging and photothermal therapy in the near-infrared region by using gold nanorods," *J. Am. Chem. Soc.* **128**, 2115–2120 (2006).
7. R. Rodriguez-Oliveros and J. A. Sanchez-Gil, "Gold nanostars as thermoplasmonic nanoparticles for optical heating," *Opt. Express* **20**, 621–626 (2012).
8. A. Mohammadi, F. Kaminski, V. Sandoghdar, and M. Agio, "Fluorescence enhancement with the optical (bi-) conical antenna," *J. Phys. Chem. C* **114**, 7372–7377 (2010).
9. H. Shen, N. Guillot, J. Rouxel, M. de la Chapelle, and T. Toury, "Optimized plasmonic nanostructures for improved sensing activities," *Opt. Express* **20**, 21278–21290 (2012).
10. A. F. Stevenson, "Solution of electromagnetic scattering problems as power series in the ratio (dimension of scatter)/wavelength," *Appl. Phys. Lett.* **24**, 1134–1141 (1953).
11. M. I. Stockman, "Nanofocusing of optical energy in tapered plasmonic waveguides," *Phys. Rev. Lett.* **93**, 137404 (2004).
12. A. Goncharenko, J. K. Wang, and Y. C. Chang, "Electric near-field enhancement of a sharp semi-infinite conical probe: Material and cone angle dependence," *Phys. Rev. B* **74**, 235442 (2006).
13. J. M. Pitarke, V. M. Silkin, E. V. Chulkov, and P. M. Echenique, "Theory of surface plasmons and surface-plasmon polaritons," *Rep. Prog. Phys.* **70**, 1–87 (2007).

14. L. Novotny and S. J. Stranick, "Near-field optical microscopy and spectroscopy with pointed probes," *Annu. Rev. Phys. Chem.* **57**, 303–331 (2006).
 15. Y. Kawata, C. Xu, and W. Denk, "Feasibility of molecular-resolution fluorescence near-field microscopy using multi-photon absorption and field enhancement near a sharp tip," *J. Appl. Phys.* **85**, 1294–1301 (1999).
 16. P. B. Johnson and R. W. Christy, "Optical constants of the noble metals," *Phys. Rev. B* **6**, 4370–4379 (1972).
 17. F. Wang and Y. Shen, "General properties of local plasmons in metal nanostructures," *Phys. Rev. Lett.* **97**, 206806 (2006).
 18. N. A. Issa and R. Guckenberger, "Optical nanofocusing on tapered metallic waveguides," *Plasmonics* **2**, 31–37 (2007).
-

1. Introduction

Surface plasmon resonance on metallic nanostructures has been extensively studied recently in their potential application in solar cell, photothermal therapy, etc. Conical nanotips have been shown to achieve better performance in the above mentioned fields, compared to smooth nanostructures like nanospheres. In solar cell application, metallic nanospheres are commonly used to enhance light absorption [1]. However, the narrow resonance spectrum of metallic nanospheres, with a limited bandwidth of about 100 nm [2], restricts the frequency range of light that can be absorbed from the entire solar spectrum (400 nm to 1200 nm). Conical nanotips have realized broadband absorption in experimental and numerical efforts [3–5], thus improving solar cell efficiency. Although broad bandwidth adsorption at the gold tip does not contribute to current generation directly, the plasmonics are scattered from the tip into the photovoltaic material. Metallic nanostructures, due to the intense and localized heat generated at plasmon resonant frequency, are suitable for cancer photothermal therapy. And it is desirable to shift resonant frequency from visible range to near infrared (NIR) range to reduce light absorbed by intrinsic chromophores in native tissue [6]. Simulation and experimental results have shown that nanotips can excite red-shifted plasmon resonance without compromising the intensity compared to gold nanospheres [7–9]. The same red-shifted broad bandwidth plasmonic excitation also suggests that multi-spectral Raman and other optical near field spectroscopy techniques can be enhanced by a conical tip.

However, a closed-form analytical theory for broadband resonance at conical nanotips that is able to quantify the bandwidth and capture the underlying mechanisms is still lacking. Existing theories failed to capture the intrinsic features of CPR due to their invalid assumptions when dealing with singular geometries. Quasi-static (long wavelength perturbation) theory [10] is frequently used to determine the plasmonic frequency of nanostructures in the literature, particularly for nanospheres, but this theory does not apply for sharp geometries with significant wavelength compression. Slender body WKB theory [11] that models a singular cone with a cylinder with a slowly varying diameter does not describe the crucial EM azimuthal field interaction around the tip of the cone and fails to capture its broadband resonance spectrum. Although a closed-form dispersion relation was given in [12], further analysis is lacking to explicitly relate broadband resonance and red-shifted resonance wavelength to material dielectric properties.

This Letter reports a rigorous analysis of the CPR resonance spectrum on conical nanotips. Our theory unveils the singular behavior of CPR on conical nanotips in the near field, captures its unique broadband resonance property and explicitly relates the resonance frequency and optimum angle to the material dielectric property. With our theory, an optimized cone is shown to have resonance frequency red-shifted and scattering spectra that span the entire solar spectrum, ten times that of a nanosphere.

2. Method description

2.1. Derivation of dispersion relationship

We solve the full Maxwell equations for localized EM field at the tip of an infinite long cone in spherical coordinate, where the origin of the coordinate resides at cone tip, as shown in the inset of Fig. 1(a). The apex angle of the cone is 2α and the cone is made of a material with a complex permittivity ε_m and a permeability μ_m surrounded by a dielectric medium with a real permittivity ε_o and a permeability μ_o , as depicted in the inset of Fig. 1(a). For the TM (transverse magnetic) mode with a magnetic field in the angular direction, the non-zero components of the EM fields are H_ϕ, E_r, E_θ , and the full set of Maxwell equations are simplified to a single scalar equation $\nabla^2 H_\phi - H_\phi/(r^2 \sin^2 \theta) + \beta_j^2 H_\phi = 0$, where $\beta_j^2 = \omega^2 \mu_j \varepsilon_j$ ($j = m, o$), ω is the frequency of the incoming light, which is the same for the CPR resonance. The radially confined harmonics within the cone-like tips ($0 < \theta < \alpha$) are $A_v^m J_{v+\frac{1}{2}}(\beta_m r) P_v^1(\cos \theta) r^{-\frac{1}{2}}$ (v is the eigenvalue), $J_{v+\frac{1}{2}}(\beta_r r)$ is the Bessel function of the first kind and $P_v^1(\cos(\theta))$ is the associate Legendre polynomial of the first kind. The corresponding harmonics for the dielectric ($\alpha < \theta < \pi$) are $A_v^o J_{v+\frac{1}{2}}(\beta_o r) P_v^1(\cos(\pi - \theta)) r^{-\frac{1}{2}}$. Note that two types of Legendre polynomials are chosen for the two media to satisfy the symmetry conditions. The θ -dependence of the EM field suggests that the EM field does not decay away from the interface, in contrast to the logarithm decay in WKB theory [11]. Applying the continuity of the field and displacement on the interface $H_\phi^m|_{\theta=\alpha} = H_\phi^o|_{\theta=\alpha}$, $E_r^m|_{\theta=\alpha} = E_r^o|_{\theta=\alpha}$ ($E_r = (\nabla \times H)_r/(-i\omega\varepsilon)$) and $\varepsilon_m E_\theta^m = \varepsilon_o E_\theta^o$ ($E_\theta = (\nabla \times H)_\theta/(-i\omega\varepsilon)$) and omitting higher order less singular plasmonic modes, a transcendental CPR dispersion relationship is obtained for the dominant eigenvalue v , with $g(\alpha, v) = \frac{f(\pi-\alpha, v)f_\theta(\alpha, v)}{f(\alpha, v)f_\theta(\pi-\alpha, v)}$, $f(\theta, v) = P_v^1(\cos \theta) \sin \theta$ and $f_\theta(\theta, v) = \frac{\partial f}{\partial \theta}(\theta, v)$

$$\frac{\varepsilon_m}{\varepsilon_o} + \frac{f(\pi - \alpha, v)f_\theta(\alpha, v)}{f(\alpha, v)f_\theta(\pi - \alpha, v)} = \frac{\varepsilon_m}{\varepsilon_o} + g(\alpha, v) = 0 \quad (1)$$

This dispersion relationship, derived using different approaches, is identical to Eq. (6) in [12]. But new underlying mechanism are to be unveiled by conformal map techniques and expansion near singular point, which will be extensively discussed in this letter.

As expected, the symmetry of Eq. (1) at $\alpha = \pi/2$ yields the classical planar plasmonic resonance condition $\varepsilon_m/\varepsilon_o + 1 = 0$ and the frequency dependence of the complex permittivity ε_m defines the planar plasmon resonant frequency ω_s with this planar resonance condition [13]. For TE (transverse electric) mode, the permittivity ratio in Eq. (1) is replaced by the permeability ratio (This ratio is close to unity for most materials in the optical range and since $Re[g(\alpha, v)]$ grows rapidly as α decreases below $\pi/2$, TE resonance can never be realized [14]). In near field, the radial component of the electric field E_r scales as $r^{\nu-1}$ (r is the radial distance from the apex of the cone), while the azimuthal magnetic field H_ϕ is less singular since it scales as r^ν ($\nu = \nu_r + i\nu_i$). The restriction that the total EM energy be finite over the entire domain requires that $-\frac{1}{2} < \nu_r < 1$ for cones [15]. The position-dependent wave-number $\kappa = \nu_i/r$ increases dramatically as CPR waves propagate toward the tip, which is found to be negative ($\nu_i < 0$) for the converging waves with speed retardation.

2.2. Conformal mapping of dispersion relationship

Equation (1) defines a conformal map $-g(\alpha, v)$ from the complex v space to the complex permittivity $\varepsilon_m/\varepsilon_o$ ($\varepsilon_m = \varepsilon_r + i\varepsilon_i$) space for cones (The dielectric permittivity ε_o of the outside medium will be set to unity for simplicity). The CPR sustainable region (grey area in Fig. 1(a)) is confined within the bold curve (the image of $\nu_r = 1$) and the horizontal axis. The point ($\varepsilon_m/\varepsilon_o = \varepsilon_{ro} = -g(\alpha, -\frac{1}{2})$) on the real line of the complex permittivity plane, which is the

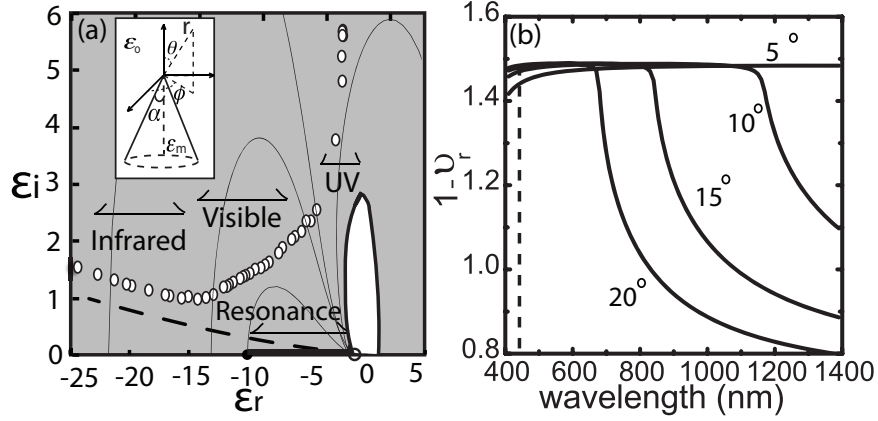


Fig. 1. (a) Conformal map in complex permittivities domain. Grey regions shows CPR sustainable region for a cone with half angle $\alpha = \pi/6$ and the contour lines correspond to constant ν_r . The branch point $dg(\alpha, \nu)/d\nu = 0$ of the conformal map is indicated as a solid dot and the limit point ($\nu_i \rightarrow \infty$) is indicated as an open circle on the negative ϵ_r axis. The bold circular contour is the image of $\nu_r = 1$. The hollow circles are empirical permittivities for gold ranging from infrared to ultraviolet wavelength [16] and the dashed curve is the Drude permittivity model for gold [13]. The band of excited frequencies for the Drude model fall at the “resonance” band between the branch point and the limit point on the real axis. (b) Intensification exponents for the Drude gold cone with half angle 5, 10, 15 and 20 degrees are plotted as solid curves. The dotted line marks the resonance peak position of a single nanosphere for comparison [2]. The broad bandwidth extends beyond the visible range for the Drude cone and the resonance frequency is red-shifted compared to gold nanospheres.

image of $\nu \rightarrow -\frac{1}{2} + 0i$, corresponding to the most singular CPR mode with vanishing wave number κ , is a branch point of the conformal map ($dg(\alpha, \nu)/d\nu = 0$, marked as a solid circle in Fig. 1(a)). Another limit point ($\epsilon_r = -1, \epsilon_i = 0$, marked as an open circle in Fig. 1(a)) of the conformal map corresponds to the common large ν_r limit for the pure dielectric (the image of the most singular mode with infinite imaginary part $\nu \rightarrow -\frac{1}{2} + i\infty$).

Maximum EM field intensification occurs at the real permittivity axis from the branch point to the limit point ($\epsilon_{r0} < \epsilon_r < -1$). The gold permittivity data of classical Drude free electron theory [13] is plotted as a dashed line in Fig. 1(a), whose imaginary permittivity decreases monotonically with frequency. At high frequency where $\epsilon_i \sim 0$ and when maximum possible intensification occurs, CPR of Drude conical nanotips hence exhibits a continuous band of resonant frequencies, whose corresponding real permittivities vary from ϵ_{r0} to -1. This continuous broad band of resonant frequency is unique to conical nanotips due to their continuous change of length scale, while finite length scale of smooth nanoparticles only exhibits discrete and sharp resonance frequency. The intensification exponents $1 - \nu_r$, computed from Eq. (1) for a Drude gold cone are shown as solid curves in Fig. 1(b) for different angles and wavelengths λ of incident light. The entire solar spectrum is excited at small angles. In contrast, the extinction spectrum for a single nanosphere [2] has a bandwidth that is 1/10 of the broadband CPR spectrum for conical nanotips. Empirical gold permittivity data which includes conduction loss due to electron interband transition [16] are also inserted as open circles in Fig. 1(a). The imaginary (loss) permittivity of gold exhibits a minimum with respect to frequency which suggests a global resonant frequency for these metals instead of the continuous band of resonant frequen-

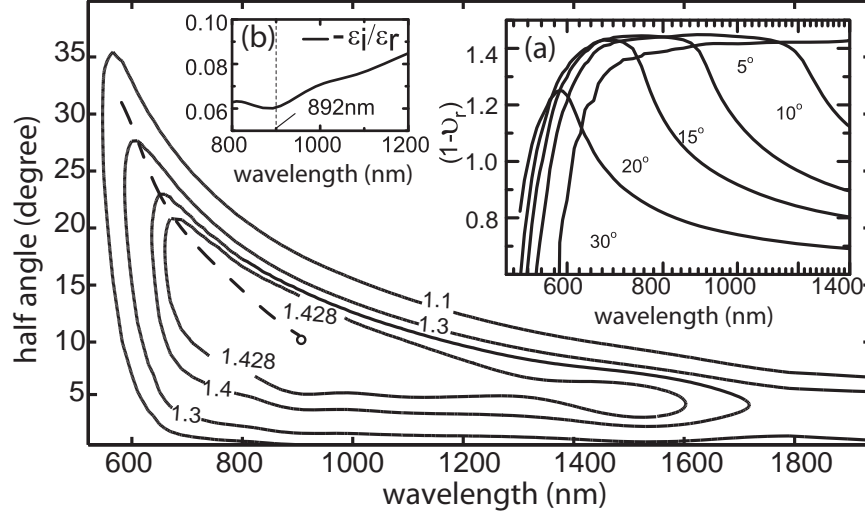


Fig. 2. Constant intensification exponent contours lines ($1 - \nu_r = 1.428, 1.4, 1.3, 1.1$) for a gold cone for empirical permittivities from [16], with different angles and incident light wavelengths, where the dashed curve connects the local resonant conditions from large angles until the global optimal angle (circle). The inset (a) plots the intensification exponent for a gold cone with different cone angles ($\alpha = 5^\circ, 10^\circ, 15^\circ, 20^\circ, 30^\circ$) and shows the CPR spectrum broadens and exhibits a red shift away from the planar plasmon resonant wavelength $\lambda_s = c/\omega_s$. The inset (b) plots the ratio of the imaginary to real permittivity for gold as a function of wavelength [16], where maximum intensification occurs at $\lambda = 892\text{nm}$.

cies for Drude-type metals. Nevertheless, the scattering feature of the cone still suggests a large bandwidth of excited/scattered light around the global resonant frequency.

2.3. Global resonance frequency

As field focusing at small cone angles can increase both the field intensity and also the conductive loss, an optimal angle is expected. Conversely, the ratio $-\epsilon_i/\epsilon_r$ of the material determines the energy loss-storage ratio of the system [17], thus should determine the global resonant frequency discussed above. Contour lines of constant EM field intensification exponent $1 - \nu_r$ computed from Eq. (1) for a gold cone with the permittivity model of [16] are shown in Fig. 2 for different angles and wavelengths λ of incident light. A global maximum in the intensification exponent exists at $\lambda = 892\text{nm}$ and $\alpha = 11^\circ$. As expected, this global resonant frequency resides at the minimum energy loss-storage ratio of gold, as shown in Fig. 2(b). The dash line connects local resonant frequency for different angles which ends at the global optimal angle. The resonance spectrum for a gold cone at different cone angles is shown in Fig. 2(a).

2.4. Asymptotic expansion

2.4.1. Branch point

Asymptotic behavior of $g(\alpha, \nu)$ in the limit of low conduction loss ($\epsilon_i/\epsilon_r \rightarrow 0$) is most relevant for both Drude-type and other metals at the IR and visible frequency range. The five curves in the complex ν plane shown in the inset of Fig. 3 are the loci of the dominant eigenvalues as a function of the half-angle α for a cone with $\epsilon_r = -182$ and for five different imaginary permittivities $\epsilon_i = 0.01, 0.5, 1, 3$ and 10 . Optimal angles for each ϵ_i , marked as solid circles

on the root loci, follows a horizontal line, which indicates that the optimal angles are only a function of ε_r for metal with low conduction loss. This invariance to conduction loss is due to a curious asymptotic behavior of the dominant eigenvalues in the no-loss dielectric limit. Their smooth loci in Fig. 3 approach the real line on left half plane ($\nu_r < 0, \nu_i = 0$) and a vertical line ($\nu_r = -\frac{1}{2}$ and $\nu_i < 0$) at the pure dielectric limit of $\varepsilon_i \rightarrow 0$, with the intersection of the two orthogonal lines occurring at $\alpha = \alpha^*$. This intersection of the two lines at $\nu = -1/2$ and $\alpha = \alpha^*$ is the image of the branch point $(\varepsilon_r, \varepsilon_i) = (\varepsilon_{ro}, 0)$. Given the wavelength of incident light and the material property, the branch point angle $\alpha = \alpha^*$ can be obtained from $dg/d\alpha(\alpha^*, -1/2) = 0$. A leading order asymptotic estimate of the branch-point angle α^* for pure dielectric with $|\varepsilon_r| \gg 1$, leads to the following explicit relation

$$\varepsilon_r = \frac{8}{\alpha^{*2} \ln(\alpha^*/8)} \quad (2)$$

However, α^* is not the optimum half angle for the zero-loss dielectric. The above asymptotic limit, shown as a bold line in Fig. 3, is actually the upper bound of a continuous range of optimum angles for metal with zero loss—all angles smaller than α^* can sustain plasmon waves with the maximum amplitude $-1/2$ for the eigenvalue ν_r . Also, the resonance bandwidth (related to ν_r) can be estimated, given this range of half cone angles. The change of optimal angle from a discrete value for finite ε_i to a continuous band for $\varepsilon_i = 0$ is reflected by the contortion of the smooth loci to a kink singularity connecting two straight lines in Fig. 3. Specific and discrete optimum angles for metal with low but finite loss ($\varepsilon_i > 0$) are depicted as solid circles in the inset and they can be better estimated by another critical point $\nu_o = -1/2 + \nu_{io}i$ at $\alpha = \alpha_o$ with a constant asymptote for the imaginary exponent $\nu_i < 0$.

2.4.2. Critical point

The optimum angle at a particular frequency can be obtained by solving Eq. (1) and optimal condition $d\nu_r/d\alpha = 0$ simultaneously at the limit of $\varepsilon_i/\varepsilon_r \rightarrow 0$ and $\varepsilon_r/\varepsilon_o \rightarrow -\infty$. Restricting ourselves to regions close to the critical point, an explicit Taylor expansion about the critical point can be carried out to yield $\nu_r + 1/2 = -i\varepsilon_i/g_\nu(\alpha_o, \nu_o)$. The optimal condition then reduces to $g_\alpha^o - g_\nu^o g_{\nu\alpha}^o/g_{\nu\nu}^o = 0$. Combination of this criterion and Eq. (1) ($\varepsilon_i = 0$) gives rise to the optimal angle α_o and the corresponding ν_{io} for any given ε_r . Good agreement between the optimal angles predicted by Eq. (1) (solid curve in Fig. 3), critical local resonance points (dotted curve in Fig. 3) and numerical data from [18] is observed in a large range of optical excitation frequency that yields a range of ε_r between -200 and -2 . Independent of ε_i , both the branch point angles and critical point angles approach zero at the large ε_r limit.

It can be shown that, for finite loss and at the limit of $\varepsilon_r/\varepsilon_o \rightarrow -\infty$, $i\varepsilon_r/g_\nu(\alpha_o, \nu_o)$ approaches a constant and hence $\nu_r + 1/2 \sim -0.693(\varepsilon_i/\varepsilon_r)$. This estimate of the dominant exponent at optimal angles for each frequency confirms that the global resonant frequency occurs at the minimum of the loss-storage ratio in Fig. 2(b). It also allows a convenient estimate of the local and global resonant frequencies from the material properties $(\varepsilon_i/\varepsilon_r)(\omega)$. As seen in Fig. 3, both the predicted exponent and optimum angle at a particular real permittivity are in good agreement with numerical values from Eq. (1).

3. Comparison with numerical results

Intensification exponent calculated from Eq. (1) can be compared to simulation data published in the literature [18]. Knowing $|E_r| \sim r^{\nu_r-1}$, we obtain the dependence of the ratio of the electric field intensity on the exponents and the geometry $E_{tip}/E_o = (r_1/r_2)^{\nu_r-1}$, where r_1 is the radial distance from the apex of the cone to the point where E_{tip} is measured and r_2 is the radial distance from the apex to the point where laser with electric field E_o impinges on the cone.

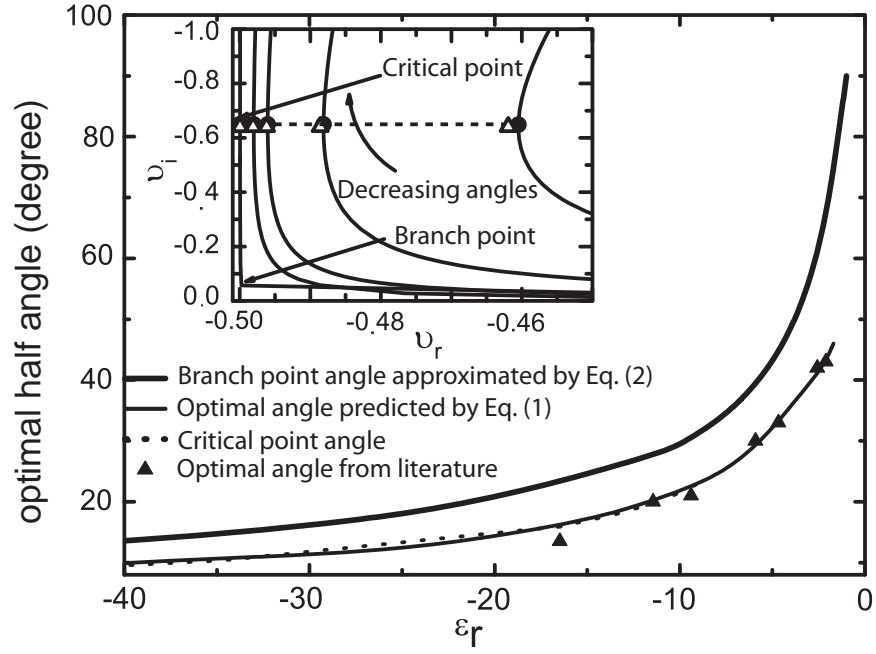


Fig. 3. Optimum angles of a gold cone at different ϵ_r corresponding to different excitation wavelength. Simulation data from the solution of the Maxwell equation [18] are compared to estimates from the branch point, the critical point and the exact solution of the CPR dispersion relationship Eq. (1). The inset depicts the dominant CPR intensification exponent as a function of the half angle for five imaginary permittivities $\epsilon_i = 0.01, 0.5, 1, 3$ and 10.0 at $\epsilon_r = -182$. The optimum angle yielding the most negative v_r is computed numerically for each ϵ_i and is marked as a solid circle on each root locus. Analytical estimate, with a ϵ_i/ϵ_r scaling, from an expansion about the critical point is shown as open triangles. At the limit of $\epsilon_i/\epsilon_r \rightarrow 0$, the eigenvalue of this optimum angle approaches the critical point at $v_o = -1/2 + v_{io}i$.

From simple geometry, $r_1 = \frac{R_1}{\sin \alpha}$ and $r_2 = \frac{R_2}{\sin \alpha}$ where $R_1 = 5$ nm is the radius of curvature of the apex and $R_2 = 300$ nm is the radius of the cylindrical wire at the far end. Figure 4 favorably compares the literature data $\log_{10}(E_{tip}/E_o)$ to our analytical estimate $(v_r - 1) \log_{10}(R_1/R_2)$, where the exponents are evaluated from Eq. (1).

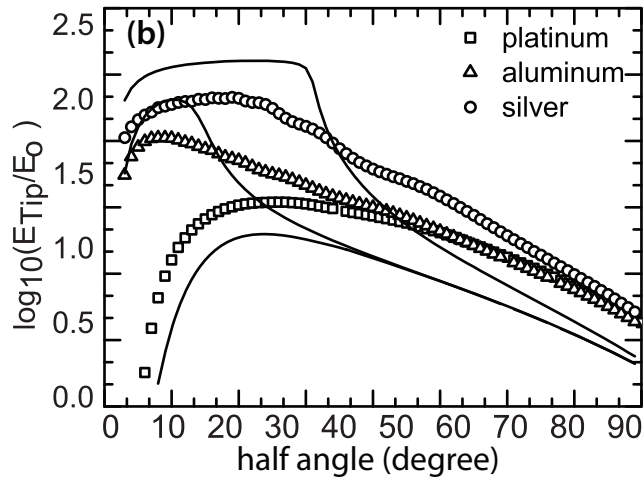
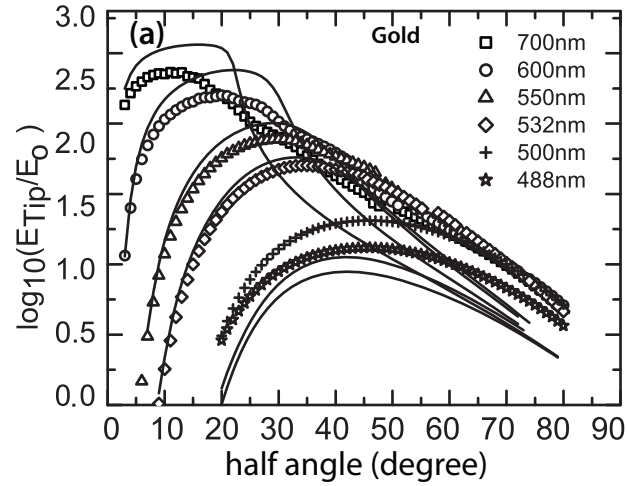


Fig. 4. (a) Comparison of theoretical intensification factor $(\nu_r - 1)\log_{10}(R1/R2)$ (solid curves) against the literature values of [18] (scattered points) for gold cones of different angles ($R1=5$ nm, $R2=300$ nm). (b) Comparison against literature data [18] for three different materials at excitation wavelength 488 nm with the same $R1$ and $R2$.

4. Conclusion

In conclusion, we have provided an analytical theory that explains the underlying mechanism of red-shifted resonance wavelength and broadband CPR spectrum at conical nanotips. Our theory predicts a continuous band of resonant frequencies for Drude-type metals and a global resonant frequency for metals with electron interband transition. Asymptotic local analysis of the CPR dispersion relation offers simple estimates of the optimal angles and resonant frequencies for materials with low loss. Intensification exponents calculated from the CPR dispersion relation are favorably compared with published simulation results. Our theory suggests that conical nanotips are ideal scattering centers for enhancing light absorption in solar cells, due to its broadband resonance and strong EM field intensity. Its red-shifted resonance bandwidth are also desirable for cancer photothermal therapy, multi-spectral Raman and other near-field spectroscopy techniques.

Acknowledgments

HCC acknowledges support from NSF Grant IDBR0852741. Helpful discussions with L-J Cheng and S. Monnieux are gratefully acknowledged.